



# CHORUS

This is the accepted manuscript made available via CHORUS. The article has been published as:

## Developing quartz and molybdenum as impedance-matching standards in the 100-Mbar regime

M. C. Marshall, A. E. Lazicki, D. Erskine, R. A. London, D. E. Fratanduono, P. M. Celliers, J. H. Eggert, F. Coppari, D. C. Swift, P. A. Sterne, H. D. Whitley, and J. Nilsen

Phys. Rev. B **99**, 174101 — Published 3 May 2019

DOI: [10.1103/PhysRevB.99.174101](https://doi.org/10.1103/PhysRevB.99.174101)

# Developing quartz and molybdenum as impedance-match standards in the 100-Mbar regime

M. C. Marshall,<sup>1,\*</sup> A. E. Lazicki,<sup>1</sup> D. Erskine,<sup>1</sup> R. A. London,<sup>1</sup>  
D. E. Fratanduono,<sup>1</sup> P. M. Celliers,<sup>1</sup> J. H. Eggert,<sup>1</sup> F. Coppari,<sup>1</sup>  
D. C. Swift,<sup>1</sup> P. A. Sterne,<sup>1</sup> H. D. Whitley,<sup>1</sup> and J. Nilsen<sup>1</sup>

<sup>1</sup>*Lawrence Livermore National Laboratory, Livermore, California 94550, USA*

## Abstract

We present quartz and molybdenum single-shock Hugoniot data to 62 Mbar and 120 Mbar, respectively. Quartz and molybdenum are attractive standard materials for Hugoniot equation-of-state impedance-matching studies. Quartz is advantageous because a reflecting shock front is supported above  $\sim 1$  Mbar whose velocity can be tracked *in situ* to very high accuracy. Molybdenum's relatively high impedance makes it a more appropriate standard for other high-impedance material studies to avoid large departures from the standard principal Hugoniot upon release or reshock into the sample. Extensive measurements already exist for both materials up to about 10 Mbar and 10 eV, but new high-energy-density facilities and techniques have extended the experimentally accessible pressure range to  $>100$  Mbar. The data presented here indicate which modern equation-of-state models can be reliably extended into newly-accessible experimental regimes.

---

\* marshall47@llnl.gov

## I. INTRODUCTION

Shock waves are commonly used to generate the high pressures and temperatures to study material response at extreme conditions ( $>1$  Mbar,  $>1$  eV). They compress materials to well-defined thermodynamic states characterized by the material's Hugoniot. The impedance-matching (IM) technique is routinely used to measure the Hugoniot of materials, historically to  $\sim 10$  Mbar pressures and  $\sim 10$  eV temperatures [1, 2]. Using this method, a sample's Hugoniot is measured relative to a standard, which has a known equation of state (EOS) [3, 4]. Using new large-scale laser facilities, it is now possible to generate quasi-steady shocks in excess of 100 Mbar, allowing access to the EOS region where the electron thermal contribution to the pressure is dominant. However, IM standards have little-to-no experimental validation at these conditions. We present Hugoniot measurements for the IM standards quartz and molybdenum (Mo) shocked to 62 Mbar and 120 Mbar, respectively. These new results extend each material's experimental Hugoniot data sets by more than a factor of two in pressure.

Quartz is a popular standard because it becomes a reflecting fluid when shocked above  $\sim 1$  Mbar, resulting in a highly-reflective shock front [5, 6] whose *in-situ* velocity can be recorded using optical diagnostics like a velocity interferometer system for any reflector (VISAR) [7]. Quartz Hugoniot and release behaviors have been studied experimentally up to 16 Mbar [3, 6]. We present new experimental Hugoniot measurements for quartz between 27 and 62 Mbar.

When there is a large impedance mismatch between the standard and sample, the off-Hugoniot behavior of the standard becomes important. To avoid large off-Hugoniot corrections, it is expedient to choose a standard that is closely impedance-matched to the material under study. Molybdenum's high impedance makes it suitable for IM experiments with materials of similarly high shock impedance [8]. We report on Hugoniot measurements for Mo between 52 and 120 Mbar.

These new quartz and Mo results use diamond as a common standard. The diamond was modeled using a comprehensive multi-phase EOS [9] that covers the high-pressure ( $>30$  Mbar) liquid regime accessed in these experiments and matches recent experimental data of full-density diamond shock compressed beyond the melt to 26 Mbar [10]. Future improvements to the diamond multi-phase EOS in our pressure range are expected based on

absolute (non-IM) Hugoniot experiments [11] using a spherically converging shock wave platform [12, 13], at which time the IM measurements detailed here can be easily updated to further improve the quartz and Mo standards.

The experiments are described in Sec. II, the IM analysis used to measure the quartz and Mo Hugoniots is discussed in Sec. III, the results and a discussion of the diamond standard EOS are presented in Sec. IV.

## II. EXPERIMENTS

The experiments were performed on the National Ignition Facility (NIF) [14] at Lawrence Livermore National Laboratory. 176 laser beams irradiated the inner walls of a gold hohlraum, producing an x-ray bath that launched a strong planar shock wave through the attached physics package [Figure 1(a)]. Data were acquired over nine experiments with total laser energies ranging from 519 to 830 kJ in 5-ns or 7.5-ns pulses (Table I). The physics package comprised a 200- $\mu\text{m}$ -thick diamond ablator, 5- $\mu\text{m}$ -thick gold preheat shield, and a 100- or 125- $\mu\text{m}$ -thick diamond baseplate serving as the IM standard. Quartz, diamond, and Mo samples were attached to the rear side of the baseplate with micron-scale layers of epoxy. The optical-grade chemical-vapor-deposition (CVD) polycrystalline diamond, the z-cut  $\alpha$ -quartz, and the Mo had densities of 3.515 g/cm<sup>3</sup>, 2.65 g/cm<sup>3</sup>, and 10.2 g/cm<sup>3</sup>, respectively.

The shock breakout times and *in-situ* velocity history in quartz were measured using VISAR. The VISAR data in Figure 1(b) are resolved spatially in the vertical direction and streaked in time to record shock motion in various regions of the target [7]. The fringe shifts in the quartz region are proportional to changes in the quartz shock velocity. Strong shock waves are reflecting in diamond [2], so an *in-situ* velocity measurement is possible in principle. However, because of diamond's high index of refraction, a strong ghost reflection from the stationary free surface is superimposed over the reflection from the quasi-steady shock wave, making the analysis difficult and potentially unreliable. Therefore, a reflecting 100-nm-thick Al coating was deposited on the diamond rear surfaces (baseplate and step), which precluded measurement of a reflecting shock but increased the accuracy of the transit-time measurements. Shot N181001 is an exception, where the diamond step was not Al coated and a quartz window was attached to its rear side, partially mitigating the strong

ghost fringe observed from a diamond free surface. The in-situ shock velocity was measured in both quartz and the diamond step, providing an additional quartz Hugoniot point at the diamond step/quartz window interface.

Average shock velocities in the Al-coated diamond and opaque Mo were determined using the measured shock transit times and initial sample thicknesses listed in Table I. There is an abrupt loss in the VISAR reflectivity when the shock breaks out of the unobstructed surfaces of the diamond baseplate and the three “steps” shown in Figure 1(b). The breakout time was identified by the steepest slope in the VISAR fringe magnitude as it drops across the material/vacuum interface. The shock transit time across the combined sample and glue layer,  $\Delta t^{\text{tot}} = t_2 - t_1$ , is the difference between the average breakout times in the baseplate adjacent to the the step,  $t_1$ , and the breakout time at the center of the step,  $t_2$ . The final  $\Delta t^{\text{tot}}$  value was the weighted average of two measurements using the two VISAR channels. Each channel had a timing uncertainty ranging from 12 to 27 ps corresponding to the temporal resolution of the streak camera, which yielded <1% total uncertainties in the transit times. The average shock velocities used in the analysis exclude the glue layer and are those across the individual samples. Individual sample thicknesses were measured using a dual confocal microscope (DCM), where the thickness and random uncertainty were the average and standard deviation, respectively, over the central measurement region relevant to the break out time measurements. The glue layer thicknesses were estimated from the step height relative to the diamond baseplate measured using a WYKO white-light interferometer. Instrument uncertainties for the DCM and WYKO measurements were  $0.63 \mu\text{m}$  and  $1.02 \mu\text{m}$ , respectively. The shock transit time across the glue layer, estimated from the glue thickness, and its shock velocity using a tabular EOS for epoxy (LEOS 5030), was subtracted from  $\Delta t^{\text{tot}}$  to give the transit time across the individual sample. The uncertainty of the glue layer thickness increases the uncertainty of the average shock velocity across the sample by approximately a factor of 2.

The quartz served as a transparent witness used to correct for shock unsteadiness in the diamond and Mo [15]. The *in-situ* shock velocity in the quartz was determined from the VISAR fringe shifts using 1.54 as the refractive index and vacuum velocity sensitivities of 19.40 and 7.80 km/s/fringe for channels A and B, respectively. Shot N181001 used 2.41 as the diamond refractive index and vacuum velocity sensitivities of 7.80 and 1.25 km/s/fringe. The laser pulse, a 5- or 7.5-ns reverse ramp, produced slowly decaying shocks in the various

samples that varied by  $\pm 3\%$  over the time period relevant to the analysis.

### III. ANALYSIS

Hugoniot analysis using the IM technique requires the shock velocities across the standard/sample interface and an EOS model for the standard. The high-pressure solid and liquid phases of diamond have been previously studied experimentally at advanced high-energy-density facilities [2, 10, 16–19] and theoretically using first-principles methods [9, 20]. The Hugoniot, the release (needed for the quartz data), and the reshock (needed for the Mo data) models for the diamond standard were taken from the LEOS 9061 table, a multiphase EOS based on density-functional theory molecular dynamics (DFT-MD) and path-integral Monte Carlo (PIMC) calculations [9]. LEOS 9061 was chosen for its consistency with recent full-density diamond Hugoniot data up to 26 Mbar [10] and experimental data of diamond releasing into quartz [10, 17]. Potential systematic errors associated with the diamond standard EOS are discussed in Section IV C.

The average shock velocities in diamond and Mo were determined using the transit time measurements given in Table I. The nonsteady waves correction [15] to these time-of-flight measurements was used to determine more accurate values of the shock velocity at the IM interface [10, 21]. The time dependent shock velocity in the opaque sample was calculated using the observed shock-velocity history in the adjacent quartz witness that experienced the same drive. Linear scaling factors  $G$  and  $F$  were used to determine the amplitude (deviation from the mean) and time dilation of the shock-velocity history in the sample relative to that of the witness. The shock velocity in the sample was described by  $U_s^{\text{samp.}}(t) = G\delta U_s^{\text{wit.}}([t - t_1]/F) + \langle U_s^{\text{samp.}} \rangle$ , where  $\langle U_s^{\text{samp.}} \rangle$  is the average shock velocity in the sample and  $\delta U_s^{\text{wit.}}(t)$  is the difference between the *in-situ* shock velocity and the average shock velocity in the witness over the time interval corresponding to the same set of perturbations as experienced by the opaque sample ( $\Delta t^{\text{samp.}}/F$ ). The linear scaling factors  $F$  and  $G$  depend on the sample, baseplate, and witness EOS, which includes sound speeds and Grüneisen parameters [15].

The choice of EOS table used to determine  $F$  and  $G$  for each material has little effect on the final Hugoniot point. This is true despite the large variation in the quartz and Mo Hugoniots from different EOS tables (curves in Figure 2). The spread in Hugoniot points

(crosses in Figure 2) from using different EOS tables to calculate  $F$  and  $G$  was well within the final error bars. The linear scaling factors used in the final analyses (Tables II and III) are those using LEOS 2210 for quartz, LEOS 9061 for diamond, and LEOS 420 for Mo.

### A. Diamond precursor study

The VISAR data for two low-intensity shots, N170227 and N170503, show motion of the diamond baseplate ahead of the shock wave and a short-lived ( $\sim 150$  ps) peak in shock velocity as it first enters the quartz. Figure 3(a) shows the free surface motion of the diamond baseplate in the unobstructed surfaces around the diamond step before shock breakout. Early diamond baseplate/quartz interface motion and increased shock velocity in the pre-compressed quartz are also observed through the transparent quartz step. These anomalies are interpreted as effects of an elastic precursor in the diamond baseplate, launched by early x-ray preheat and expansion of the 5- $\mu\text{m}$ -thick gold layer. In the high-intensity shots, the main shock wave caught up to the precursor inside the baseplate and these anomalous effects were not observed. For the two affected shots, the precursor entered the three samples before the main shock overtook it. This caused precompression of the diamond baseplate and the first  $\sim 10\text{-}30$   $\mu\text{m}$  of the three samples. The precursor effect was potentially problematic both for the nonsteady waves correction, because the degree of precompression varied between the three samples, and for the IM analysis, because it altered the pre-shock conditions of the samples, preventing true principal Hugoniot measurements.

Simulations were done using the HYDRA radiation/hydrodynamics code [22] to better understand the precompression effects and account for them in the Hugoniot analysis. A material strength model for diamond (Ref. [23]) with a shear modulus of 5.38 Mbar and a yield strength of 0.78 Mbar was used to simulate the elastic precursor wave. When combined with the bulk modulus of 4.44 Mbar from the EOS (LEOS 9061), the shear strength allows low pressure elastic waves to propagate at a velocity of 18.2 km/s. The N170503 experiment was simulated both with and without material strength in diamond. The velocity histories are shown for the diamond and quartz samples along with the experimental data in Figure 3(b). The increased shock velocity in the first  $\sim 150$  ps in the quartz sample is seen in both the experiment (solid black curve) and the simulation that includes strength in diamond (solid blue curve). The simulation without strength (dotted blue curve) does

not show the increased shock velocity. The precompressed region in the stepped diamond sample was not directly observed experimentally because of the rear aluminum coating.

The simulated shock velocity histories with and without strength agree after the main shock overtakes the precompression wave. Despite the clear effects of the precursor on the initial velocity histories, the simulations indicate that the effect on the average shock velocity in diamond (the experimental observable) is negligible. The average shock velocity in the precompressed diamond sample was only  $\sim 0.1\%$  higher than that without strength, much less than the experimental uncertainty of  $\sim 1\%$ . This result allowed us to ignore the small precompressed region in the quartz witness, effectively treating it as a small perturbation similar to a glue or oil layer [24]. The shock velocity in quartz after the main shock caught up was extrapolated backwards to the diamond-baseplate interface (dashed black line). The extrapolated quartz shock velocity was used for impedance matching and the nonsteady waves analysis.

Shots N180411 and N180611 replicated the Hugoniot states reached in the two affected shots, however, the laser pulse shape was adjusted and the thickness of the diamond baseplate and gold layer were increased to eliminate the precursor problem. The Hugoniot data from the affected and unaffected shots reasonably agree (four lowest pressure data points in Figure 4), giving confidence in our treatment of the precursor.

## IV. RESULTS

The new Hugoniot data for quartz and Mo are listed in Tables II and III, respectively.

### A. Quartz

Ten new Hugoniot measurements using a diamond standard for quartz shocked to 27 - 62 Mbar are shown in Figure 4. Two previously unpublished data points by Celliers and Fratanduono (N141209 and N150512) that used the same experimental platform but with an aluminum standard [25] are also presented. These new results reach  $\sim 3.5\times$  higher pressures than previously published experimental data acquired at the Z facility [3, 6, 26] and using underground nuclear explosions [27]. The aluminum to quartz impedance-matching analysis in the Trunin nuclear experiment [27] was redone here using the more recent aluminum

EOS [25] used for the two new quartz data. Estimates of the systematic uncertainty in the Al impedance-matching standard [25] were also included in the error bars for these two new quartz data.

First principles molecular dynamics (FPMD) calculations by Desjarlais, Knudson, and Cochrane [26] and Sjostrom and Crockett [28] predict an overall stiffening of the Hugoniot compared to *SESAME* 7385 (average atom model). This reduced compressibility is generally observed with the new data. The FPMD model by Sjostrom and Crockett [28] agrees well with the quartz Hugoniot data over the entire pressure range of the Z-data set and this work. Their calculations employed an orbital-free extension to Kohn-Sham DFT to simulate liquid SiO<sub>2</sub> at the higher densities (5-15 g/cm<sup>3</sup>) and temperatures (>8 eV) relevant to the experimental data [28]. The exponential fit to the Z facility data and FPMD calculations from Ref. 26, which was extrapolated beyond its upper bound of 30 Mbar in Figure 4, is slightly stiffer than our results but they do agree, within our uncertainty, above ~45 Mbar. LEOS 2210 is adequate for our new data but too compressible when compared to the Z facility data [3, 6, 26].

## B. Molybdenum

Four Hugoniot measurements were acquired for Mo shocked between 52 and 120 Mbar. The data are shown in Figure 5 with previously published gas gun data up to 5 Mbar [29, 30] and data obtained using underground nuclear explosions [27, 30–34], which reached 40 Mbar. The data that used aluminum standards [30, 32] were reanalyzed using the more recent analytic EOS for aluminum [25]. The data are compared to five EOS tables, LEOS 420 and *SESAME* 2980, 2981, 2983 and 2984 [35]. The previously published data and all four new Mo Hugoniot points agree with LEOS 420 and *SESAME* 2981. LEOS 420 was made using a quotidian EOS (QEOS)-like model [36] with some non-QEOS additions from Young and Corey [37]. *SESAME* 2981 was made using the DFT-based method INFERNO [38] and was the EOS for Mo standards in previous studies [8, 32].

### C. Diamond EOS discussion

The above results assumed the LEOS 9061 table [9] for the diamond EOS because it is the most advanced of the available tables and it best agrees with the highest precision experimental data for full-density diamond [2, 10, 16] as shown in Figure 6(a). We did not include a systematic uncertainty in the diamond EOS because, in the absence of experimental data in our pressure range [gray-shaded area in Figure 6(a)], the magnitude of the uncertainty is unknown. We considered using the spread in various diamond EOS tables as a bound on the uncertainty, but this is not necessarily accurate and it is clear that LEOS 9061 best agrees with the existing data at lower pressure. We instead present a sensitivity study, where we repeated the quartz and Mo Hugoniot analyses using *SESAME* 7834 and LEOS 64 for the diamond EOS to estimate potential systematic effects associated with the diamond standard.

All of the quartz and Mo data analyzed using *SESAME* 7834 for the diamond EOS [blue triangles in Figure 6(b) and (c)] are in agreement with the analyses using LEOS 9061 (black circles). Using LEOS 64 for the diamond EOS produces quartz and Mo data (red squares) that are systematically stiffer than the results that assume LEOS 9061. This is expected because the LEOS 64 diamond Hugoniot [red dashed curve in Figure 6(a)] is stiffer than the LEOS 9061 Hugoniot (black solid curve) over the pressure range of shocked diamond in these experiments (gray shaded area). The quartz and Mo results using LEOS 64 agree with those using LEOS 9061 for all shots except the lowest pressure data from N170503 near 28 Mbar in quartz and 53 Mbar in Mo. While using LEOS 64 brings the quartz data at 25-30 Mbar closer to the two FPMD calculations [26] [magenta asterisks in Figure 6(b)], we have less confidence in the LEOS 64 Hugoniot at the corresponding diamond pressures of 33-37 Mbar because it is significantly stiffer than the experimental diamond data near 25 Mbar [Figure 6(a)].

The diamond, quartz, and Mo shock velocities are given in Tables II and III so that the IM analyses can be redone pending future improvements to the diamond EOS model.

## V. CONCLUSIONS

The quartz and Mo Hugoniot data were measured at unprecedented pressures in the  $\sim 100$ -Mbar regime. These new measurements help develop quartz and Mo as impedance-match standards to more than double the highest pressures that were previously published. The pressure-temperature conditions reached in these experiments access a regime above melting but below peak shock compressibility, where the Hugoniot is affected by the atomic shell structure. The LEOS 420 (Mo) and LEOS 2210 (quartz) models show that the electron thermal contribution to the total pressure is dominant under the conditions in our experiments, while the cold curve and ion thermal components are not negligible. Both the existing and new quartz data are well represented by the FPMD model of Sjoström and Crockett [28] and the Mo Hugoniot data are best represented by LEOS 420 and *SESAME* 2981.

## ACKNOWLEDGMENTS

This work was performed under the auspices of the U.S. Department of Energy by Lawrence Livermore National Laboratory under Contract DE-AC52-07NA27344.

This document was prepared as an account of work sponsored by an agency of the United States government. Neither the United States government nor Lawrence Livermore National Security, LLC, nor any of their employees makes any warranty, expressed or implied, or assumes any legal liability or responsibility for the accuracy, completeness, or usefulness of any information, apparatus, product, or process disclosed, or represents that its use would not infringe privately owned rights. Reference herein to any specific commercial product, process, or service by trade name, trademark, manufacturer, or otherwise does not necessarily constitute or imply its endorsement, recommendation, or favoring by the United States government or Lawrence Livermore National Security, LLC. The views and opinions of authors expressed herein do not necessarily state or reflect those of the United States government or Lawrence Livermore National Security, LLC, and shall not be used for

advertising or product endorsement purposes.

---

- [1] M. A. Barrios, D. G. Hicks, T. R. Boehly, D. E. Fratanduono, J. H. Eggert, P. M. Celliers, G. W. Collins, and D. D. Meyerhofer, *Phys. Plasmas* **17**, 056307 (2010).
- [2] D. G. Hicks, T. R. Boehly, P. M. Celliers, D. K. Bradley, J. H. Eggert, R. S. McWilliams, R. Jeanloz, and G. W. Collins, *Phys. Rev. B* **78**, 174102 (2008).
- [3] M. D. Knudson and M. P. Desjarlais, *Phys. Rev. B* **88**, 184107 (2013).
- [4] M. D. Knudson, M. P. Desjarlais, and A. Pribram-Jones, *Phys. Rev. B* **91**, 224105 (2015).
- [5] D. G. Hicks, T. R. Boehly, J. H. Eggert, J. E. Miller, P. M. Celliers, and G. W. Collins, *Phys. Rev. Lett.* **97**, 025502 (2006).
- [6] M. D. Knudson and M. P. Desjarlais, *Phys. Rev. Lett.* **103**, 225501 (2009).
- [7] P. M. Celliers, D. K. Bradley, G. W. Collins, D. G. Hicks, T. R. Boehly, and W. J. Armstrong, *Rev. Sci. Instrum.* **75**, 4916 (2004).
- [8] C. E. Ragan, *Phys. Rev. A* **29**, 1391 (1984).
- [9] L. X. Benedict, K. P. Driver, S. Hamel, B. Militzer, T. Qi, A. A. Correa, A. Saul, and E. Schwegler, *Phys. Rev. B* **89**, 224109 (2014).
- [10] M. C. Gregor, D. E. Fratanduono, C. A. McCoy, D. N. Polsin, A. Sorce, J. R. Rygg, G. W. Collins, T. Braun, P. M. Celliers, J. H. Eggert, D. D. Meyerhofer, and T. R. Boehly, *Phys. Rev. B* **95**, 144114 (2017).
- [11] D. C. Swift, A. L. Kritcher, A. E. Lazicki, J. A. Hawreliak, T. Döppner, B. Bachmann, S. D. Rothman, N. Kostinski, B. Maddox, D. Kraus, J. Nilsen, M. Martin, A. M. Saunders, H. D. Whitley, G. W. Collins, S. H. Glenzer, and R. W. Falcone (unpublished).
- [12] D. C. Swift, A. L. Kritcher, J. A. Hawreliak, A. Lazicki, A. MacPhee, B. Bachmann, T. Döppner, J. Nilsen, G. W. Collins, S. Glenzer, S. D. Rothman, D. Kraus, and R. W. Falcone, *Rev. Sci. Instrum.* **89**, 053505 (2018).
- [13] T. Döppner, D. C. Swift, A. L. Kritcher, B. Bachmann, G. W. Collins, D. A. Chapman, J. Hawreliak, D. Kraus, J. Nilsen, S. Rothman, L. X. Benedict, E. Dewald, D. E. Fratanduono, J. A. Gaffney, S. H. Glenzer, S. Hamel, O. L. Landen, H. J. Lee, S. LePape, T. Ma, M. J. MacDonald, A. G. MacPhee, D. Milathianaki, M. Millot, P. Neumayer, P. A. Sterne, R. Tommasini, and R. W. Falcone, *Phys. Rev. Lett.* **121**, 025001 (2018).

- [14] E. I. Moses, R. N. Boyd, B. A. Remington, C. J. Keane, and R. Al-Ayat, *Phys. Plasmas* **16**, 041006 (2009).
- [15] D. E. Fratanduono, D. H. Munro, P. M. Celliers, and G. W. Collins, *J. Appl. Phys.* **116**, 033517 (2014).
- [16] M. D. Knudson, M. P. Desjarlais, and D. H. Dolan, *Science* **322**, 1822 (2008).
- [17] M. Millot, P. M. Celliers, P. A. Sterne, L. X. Benedict, A. A. Correa, S. Hamel, S. J. Ali, K. L. Baker, L. F. Berzak Hopkins, J. Biener, G. W. Collins, F. Coppari, L. Divol, A. Fernandez-Panella, D. E. Fratanduono, S. W. Haan, S. Le Pape, N. B. Meezan, A. S. Moore, J. D. Moody, J. E. Ralph, J. S. Ross, J. R. Rygg, C. Thomas, D. P. Turnbull, C. Wild, and J. H. Eggert, *Phys. Rev. B* **97**, 144108 (2018).
- [18] R. F. Smith, J. H. Eggert, R. Jeanloz, T. S. Duffy, D. G. Braun, J. R. Patterson, R. E. Rudd, J. Biener, A. E. Lazicki, A. V. Hamza, J. Wang, T. Braun, L. X. Benedict, P. M. Celliers, and G. W. Collins, *Nature* **511**, 330 (2014).
- [19] J. H. Eggert, D. G. Hicks, P. M. Celliers, D. K. Bradley, R. S. McWilliams, R. Jeanloz, J. E. Miller, T. R. Boehly, and G. W. Collins, *Nat. Phys.* **6**, 40 (2010).
- [20] A. A. Correa, L. X. Benedict, D. A. Young, E. Schwegler, and S. A. Bonev, *Phys. Rev. B* **78**, 024101 (2008).
- [21] D. E. Fratanduono, P. M. Celliers, D. G. Braun, P. A. Sterne, S. Hamel, A. Shamp, E. Zurek, K. J. Wu, A. E. Lazicki, M. Millot, and G. W. Collins, *Phys. Rev. B* **94**, 184107 (2016).
- [22] M. M. Marinak, G. D. Kerbel, N. A. Gentile, O. Jones, D. Munro, S. Pollaine, T. R. Dittrich, and S. W. Haan, *Phys. Plasmas* **8**, 2275 (2001).
- [23] D. Orlikowski, A. A. Correa, E. Schwegler, and J. E. Klepeis, *AIP Conf. Proc.* **955**, 247 (2007).
- [24] A. Lazicki, R. A. London, F. Coppari, D. Erskine, H. D. Whitley, K. J. Caspersen, D. E. Fratanduono, M. A. Morales, P. M. Celliers, J. H. Eggert, M. Millot, D. C. Swift, G. W. Collins, S. O. Kucheyev, J. I. Castor, and J. Nilsen, *Phys. Rev. B* **96**, 134101 (2017).
- [25] P. M. Celliers, G. W. Collins, D. G. Hicks, and J. H. Eggert, *J. Appl. Phys.* **98**, 113529 (2005).
- [26] M. P. Desjarlais, M. D. Knudson, and K. R. Cochrane, *J. Appl. Phys.* **122**, 035903 (2017).
- [27] R. F. Trunin, *Phys.-Usp.* **37**, 1123 (1994).
- [28] T. Sjostrom and S. Crockett, *Phys. Rev. B* **92**, 115104 (2015).

- [29] R. S. Hixson and J. N. Fritz, *J. Appl. Phys.* **71**, 1721 (1992).
- [30] A. C. Mitchell, W. J. Nellis, J. A. Moriarty, R. A. Heinle, N. C. Holmes, R. E. Tipton, and G. W. Repp, *J. Appl. Phys.* **69**, 2981 (1991).
- [31] C. E. Ragan, M. G. Silbert, and B. C. Diven, *J. Appl. Phys.* **48**, 2860 (1977).
- [32] C. E. Ragan, *Phys. Rev. A* **25**, 3360 (1982).
- [33] L. Al'tshuler, A. Bakanova, I. Dudoladov, E. A. Dynin, R. F. Trunin, and B. S. Chekin, *J. Appl. Mech. Tech. Phys.* **22**, 145 (1981).
- [34] R. F. Trunin, M. V. Panov, and A. B. Medvedev, *Pis'ma Zh. Eksp. Teor. Fiz.* **62**, 572 (1995).
- [35] S. P. Lyon and J. D. Johnson, "LANL Report No. LA-UR-92-3407," (1992).
- [36] R. M. More, K. H. Warren, D. A. Young, and G. B. Zimmerman, *Phys. Fluids* **31**, 3059 (1988).
- [37] D. A. Young and E. M. Corey, *J. Appl. Phys.* **78**, 3748 (1995).
- [38] D. A. Liberman, *Phys. Rev. B* **20**, 4981 (1979).

## FIGURES

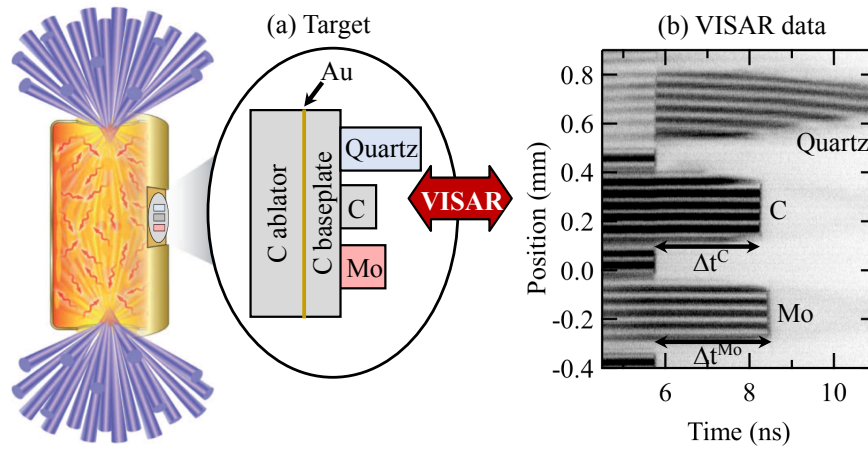


FIG. 1. (a) NIF hohlraum target and physics package with quartz, diamond (C) and Mo samples attached to the diamond baseplate (impedance-match standard) and (b) VISAR data for NIF shot N161002.

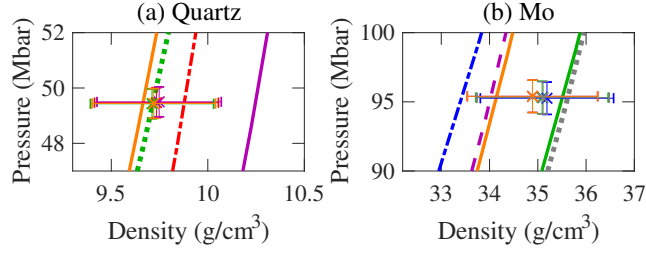


FIG. 2. Spread in Hugoniot data for shot N160414 when using various EOS tables to determine parameters  $F$  and  $G$  for the nonsteady waves correction. While the spread in EOS tables (curves) is large, their effect on  $F$  and  $G$ , and the final Hugoniot points (crosses) is minimal compared to the error bars. (a) EOS tables *SESAME* 7383 (dashed-dotted red), *SESAME* 7385 (solid purple), EOS from Sjostrom and Crockett (dotted green), and LEOS 2210 (solid orange) were tested for quartz and (b) *SESAME* 2980 (solid green), *SESAME* 2981 (dashed purple), *SESAME* 2983 (dashed-dotted blue), *SESAME* 2984 (dotted gray), and LEOS 420 (solid orange) were tested for Mo.

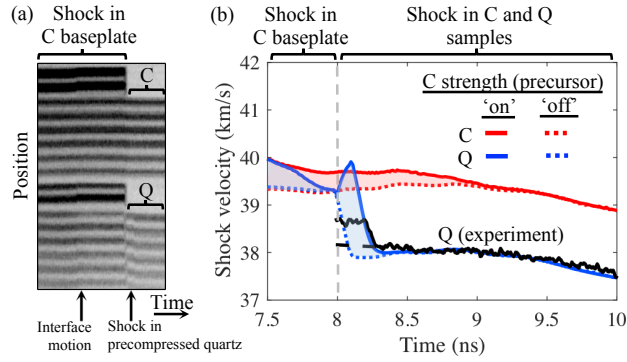


FIG. 3. (a) VISAR image showing evidence of the precursor. The arrival of the precursor at the diamond (C) free surface and diamond/quartz (Q) interface is marked by the arrow labeled “interface motion”. (b) Shock velocity histories from the experiment (N170503) and HYDRA simulations with and without strength in the diamond. The shaded region shows differences in shock velocity due to the precursor.

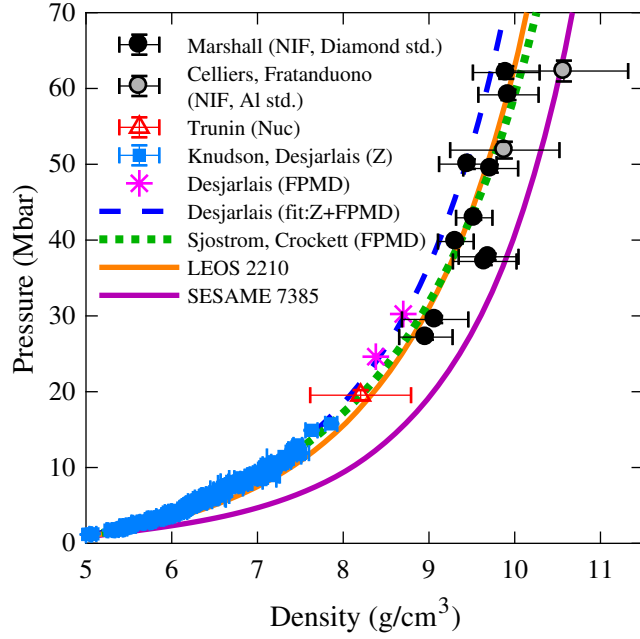


FIG. 4. New quartz Hugoniot data using a diamond standard (black circles) and an aluminum standard (gray circles). Also shown are data acquired at the Sandia Z-machine (blue squares) [3, 6, 26], FPMD calculations from Desjarlais, Knudson, and Cochran (magenta asterisks) [26], Sjoström and Crockett (dotted green) [28], and tabular EOS models. The fit to the Z-data and FPMD calculations presented by Desjarlais *et al.* [26] was extrapolated beyond its upper bound, 30 Mbar, represented by the dashed blue curve.

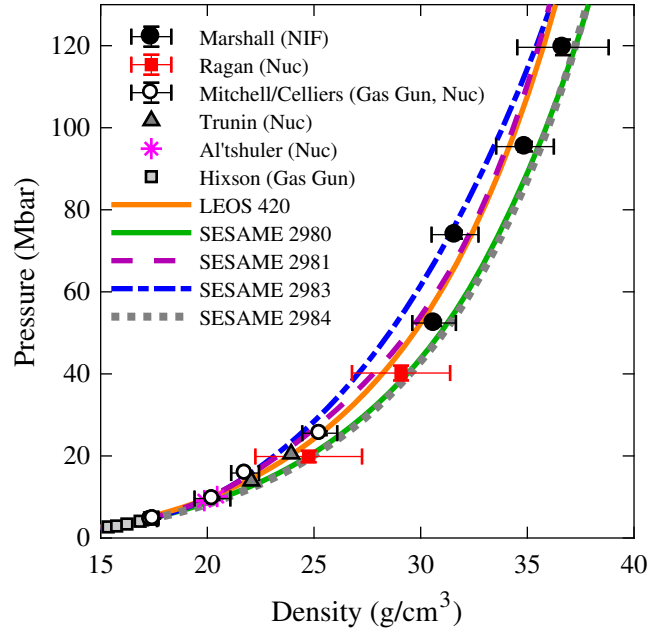


FIG. 5. New Mo Hugoniot data using a diamond standard (black circles) shown with previous data published by Ragan *et al.* (red squares) [31, 32], Hixson and Fritz (gray squares) [29], Trunin *et al.* (gray triangles) [27, 34], Mitchell *et al.* (white circles) [30] reanalyzed by Celliers *et al.* in Ref. [25], and Al'tshuler *et al.* (magenta asterisks) [33].

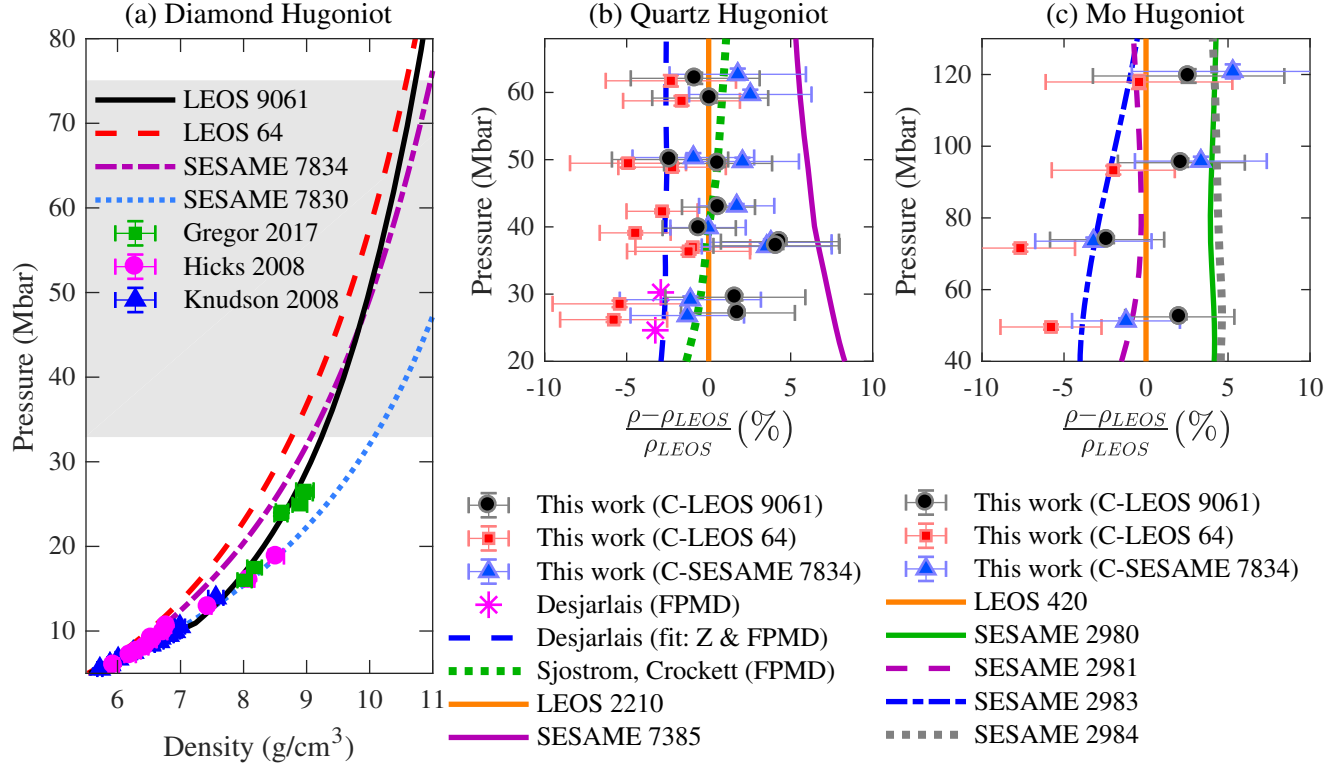


FIG. 6. (a) Hugoniot data and models for full-density ( $\rho_0 = 3.515 \text{ g/cm}^3$ ) diamond. The gray shaded region represents the pressure range of the shocked diamond in these experiments. Analyses of the quartz (b) and Mo (c) Hugoniot data using LEOS 9061 (black circles), LEOS 64 (red squares), and *SESAME* 7834 (blue triangles) as the diamond standard EOS. Subplots (b) and (c) show pressure as a function of the percent difference in density ( $\rho$ ) compared to that of LEOS 2210 for quartz and LEOS 420 for Mo.

## TABLES

TABLE I. Total laser energy ( $E^{\text{Laser}}$ ), where shots N160414, N161002, N170801, and N170808 used a 5-ns pulse and the remaining shots used a 7.5 ns pulse. Diamond (C) and Mo target thicknesses ( $x$ ), shock transit times ( $\Delta t$ ), and average velocities ( $\langle U_S \rangle$ ) of the individual samples (samp) and combined sample and glue layer (tot). \*The *in-situ* shock velocity in diamond was measured for shot N181001.

Shot	$E^{\text{Laser}}$ (kJ)	Sample	$x^{\text{tot.}}$ ( $\mu\text{m}$ )	$\Delta t^{\text{tot.}}$ (ns)	$x^{\text{samp.}}$ ( $\mu\text{m}$ )	$\langle U_S^{\text{samp.}} \rangle$ (km/s)
N160414	663	C	148.90 $\pm$ 1.02	2.965 $\pm$ 0.011	148.70 $\pm$ 0.66	50.22 $\pm$ 0.35
		Mo	102.70 $\pm$ 1.08	2.887 $\pm$ 0.011	100.70 $\pm$ 0.66	35.30 $\pm$ 0.28
N161002	820	C	135.14 $\pm$ 1.04	2.471 $\pm$ 0.015	136.78 $\pm$ 0.65	55.35 $\pm$ 0.50
		Mo	105.38 $\pm$ 1.67	2.658 $\pm$ 0.015	101.00 $\pm$ 1.02	39.01 $\pm$ 0.48
N170227	685	C	134.80 $\pm$ 1.03	3.033 $\pm$ 0.010	135.29 $\pm$ 0.64	44.61 $\pm$ 0.33
		Mo	100.49 $\pm$ 1.09	3.193 $\pm$ 0.010	101.50 $\pm$ 0.75	31.79 $\pm$ 0.25
N170503	519	C	135.18 $\pm$ 1.04	3.497 $\pm$ 0.010	133.96 $\pm$ 0.64	38.62 $\pm$ 0.29
		Mo	101.87 $\pm$ 1.04	3.740 $\pm$ 0.010	98.82 $\pm$ 0.67	26.93 $\pm$ 0.20
N170801	827	C	135.33 $\pm$ 1.03	2.483 $\pm$ 0.010	134.61 $\pm$ 0.64	54.47 $\pm$ 0.42
N170808	705	C	135.61 $\pm$ 1.13	2.688 $\pm$ 0.010	134.40 $\pm$ 0.63	50.38 $\pm$ 0.41
N180411	714	C	135.91 $\pm$ 1.02	3.052 $\pm$ 0.015	134.86 $\pm$ 0.64	44.49 $\pm$ 0.37
N180611	573	C	134.65 $\pm$ 1.46	3.422 $\pm$ 0.010	132.50 $\pm$ 1.08	39.27 $\pm$ 0.40
N181001*	772	C	-	-	-	-

TABLE II. Quartz Hugoniot data from impedance matching (IM) with a standard (Stan) of diamond (C) or aluminum (Al). Shock velocities ( $U_S$ ) at the IM interface were measured *in situ* using VISAR for quartz (Q) and inferred using the nonsteady waves correction for the standard with linear scaling factors  $F$  and  $G$ . These velocities were used in the IM analysis to determine the particle velocity ( $u_p$ ), pressure ( $P$ ), and density ( $\rho$ ) on the quartz Hugoniot. \*The *in-situ* shock velocity in diamond was measured for shot N181001.

Shot:Stan	$F(\frac{dStan}{dQ})$	$G(\frac{dStan}{dQ})$	$\delta U_S^Q$	$U_S^{Stan}$	$U_S^Q$	$u_p^Q$	$P^Q$	$\rho^Q$
	-	-	(km/s)	(km/s)	(km/s)	(km/s)	(Mbar)	(g/cm <sup>3</sup> )
N160414:C	1.02	0.964	0.81	51.00±0.35	50.65±0.25	36.84±0.39	49.44±0.54	9.720±0.320
N161002:C	1.01	0.963	1.13	56.43±0.50	56.57±0.25	41.43±0.54	62.10±0.83	9.901±0.389
N170227:C	1.04	0.970	0.81	45.39±0.33	44.30±0.25	32.19±0.36	37.80±0.44	9.695±0.349
N170503:C	1.04	0.968	0.58	39.18±0.29	38.17±0.25	26.89±0.31	27.20±0.34	8.964±0.311
N170801:C	1.02	0.960	0.81	55.25±0.42	55.18±0.25	40.45±0.46	59.16±0.69	9.927±0.351
N170808:C	0.99	0.973	0.77	51.13±0.41	51.22±0.25	36.86±0.45	50.02±0.63	9.453±0.335
N180411:C	1.03	0.970	0.58	45.05±0.37	43.98±0.25	31.90±0.40	37.18±0.48	9.650±0.371
N180611:C	1.03	0.971	1.37	40.60±0.40	39.67±0.25	28.09±0.43	29.53±0.47	9.072±0.387
N181001a:C*	-	-	-	47.89±0.16	47.38±0.25	34.20±0.18	42.94±0.27	9.528±0.212
N181001b:C*	-	-	-	46.25±0.16	45.82±0.25	32.78±0.18	39.81±0.26	9.313±0.208
N141209:Al	0.92	0.990	0.45	50.70±0.43	51.71±0.44	37.85±0.78	51.87±1.10	9.885±0.637
N150512:Al	0.97	0.970	0.46	55.39±0.51	56.00±0.44	41.98±0.90	62.30±1.38	10.57±0.750

TABLE III. Mo Hugoniot data from impedance matching (IM) with a diamond (C) standard. Shock velocities ( $U_S$ ) at the IM interface were inferred using the nonsteady waves correction; the diamond shock velocity history was determined first using the information in Table II. These velocities were used in the IM analysis to determine the particle velocity ( $u_p$ ), pressure ( $P$ ), and density ( $\rho$ ) on the Mo Hugoniot.

Shot:Stan	$F(\frac{d\text{Mo}}{dC})$	$G(\frac{d\text{Mo}}{dC})$	$\delta U_S^C$ (km/s)	$U_S^C$ (km/s)	$U_S^{\text{Mo}}$ (km/s)	$u_p^{\text{Mo}}$ (km/s)	$P^{\text{Mo}}$ (Mbar)	$\rho^{\text{Mo}}$ (g/cm <sup>3</sup> )
N160414:C	0.770	0.753	1.29	51.00±0.35	36.27±0.28	25.58±0.31	95.40±1.17	34.89±1.35
N161002:C	0.753	0.757	1.58	56.43±0.50	40.20±0.48	28.94±0.44	119.6±1.90	36.67±2.14
N170227:C	0.840	0.730	1.18	45.39±0.33	32.65±0.25	22.03±0.28	73.94±0.97	31.61±1.10
N170503:C	0.787	0.742	1.04	39.18±0.29	27.70±0.20	18.40±0.24	52.40±0.70	30.63±1.02